PAPER

Antenna-plasma coupling calculations for the ITER low-field side reflectometer

IOP Publishing | International Atomic Energy Agency Nuclear Fusion

Nucl. Fusion **58** (2018) 126014 (11pp) https://doi.org/10.1088/1741-4326/aadea1

Antenna-plasma coupling calculations for the ITER low-field side reflectometer

G.J. Kramer, E.J. Valeo, A. Zolfaghari and N. Bertelli

Princeton Plasma Physics Laboratories, PO box 451, Princeton, NJ 08543, United States of America

E-mail: gkramer@pppl.gov

Received 16 February 2018, revised 12 July 2018
Accepted for publication 4 September 2018
Published 27 September 2018

Abstract

The antenna–plasma coupling for the ITER low-field side reflectometer system (LFSR) was studied using the hybrid 3D reflectometer simulation code FWR3D, in which full-wave, paraxial, and free-space solvers are used for speed and accuracy. Reflections from equilibrium profiles were simulated to study and optimize the power that is coupled the receiving antenna. At the optimal coupling, the effects of density fluctuations were also calculated, showing that the density fluctuations decrease the average coupling by as much as 6 dB. This study indicates that after some minor changes to the location of the proposed antennas, the antenna–plasma coupling of the ITER LFSR provides a sufficient basis from which to design and build a reflectometer system that meets the specifications requested by ITER.

Keywords: ITER, reflectometry, antenna–plasma coupling

(Some figures may appear in colour only in the online journal)

1. Introduction

One of the key diagnostics on ITER is the low-field side reflectometer (LFSR), whose primary tasks are to measure edge density profiles and fluctuations [1]. Reflectometry is a microwave based technique to measure electron density profiles and fluctuations in fusion plasmas [2]. Currently, a fast-swept system over a frequency range from 30 to 165 GHz is under consideration for the ITER LFSR whereby the microwave sources and receivers are located in the diagnostic hall and are connected to the antennas inside the vacuum vessel by a transmission line consisting of 40 m of circular wave guide, up to 13 miter bends, and a Gaussian telescope.

Three conditions have to be satisfied for the reliable operation of this system: (i) high-power ($\gtrsim$100 mW) fast-tunable micro-wave sources, (ii) low losses in the transmission line, and (iii) a good coupling between the antennas and the plasma.

The first two conditions—high-power, fast-tunable microwave sources and low-loss transmission lines—can be engineered and optimized in the lab. The antenna–plasma coupling, however, cannot be studied and/or optimized experimentally before ITER plasmas become available because in current machines the plasma size, densities, and magnetic fields are too low to obtain plasma reflections over the 30–165 GHz frequency range that is needed in ITER (which follows directly from the magnetic field (5.4 T at the magnetic axis and the expected electron density of 10^{20} m^{-3}). A profile reflectometer that is swept fast over a much smaller range (30–75 GHz) has successfully been made operational in DIII-D [3].

In reflectometer bench-tests, the plasma is usually replaced by a mirror of some shape (flat, curved, with or without corrugations) to simulate the antenna–plasma coupling. Although these mirror-tests are a necessary part of reflectometer design, they cannot give information on aspects of the antenna–plasma coupling due to refraction and density fluctuation effects in the plasma. These plasma effects usually degrade the antenna–plasma coupling, and should be taken into account in the reflectometer design.

An alternative way to study the antenna–plasma coupling is to use computer simulations. Reflectometer response simulations have been performed on a regular basis to interpret density fluctuation measurements [4, 5]. These simulations, however, were performed in a single poloidal plane, reducing the simulations to a 2D problem which is a valid approach for physics studies in toroidal symmetric devices [6]. The antenna–plasma coupling problem, however, cannot be treated with such 2D-codes because the antennas have finite radiation patterns and the plasma is curved in both poloidal and

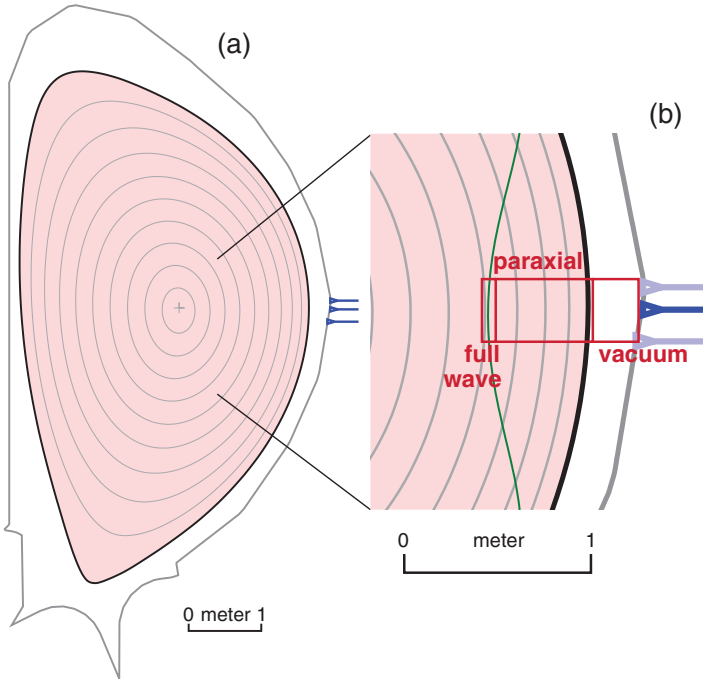

Figure 1. (*a*) ITER plasma shape and the antenna array used in this paper for the antenna coupling of the LFSR system and (*b*) a close-up of the various simulation regimes used in the FWR3D code with the reflection layer indicated with the green line. The contours indicate minor radii.

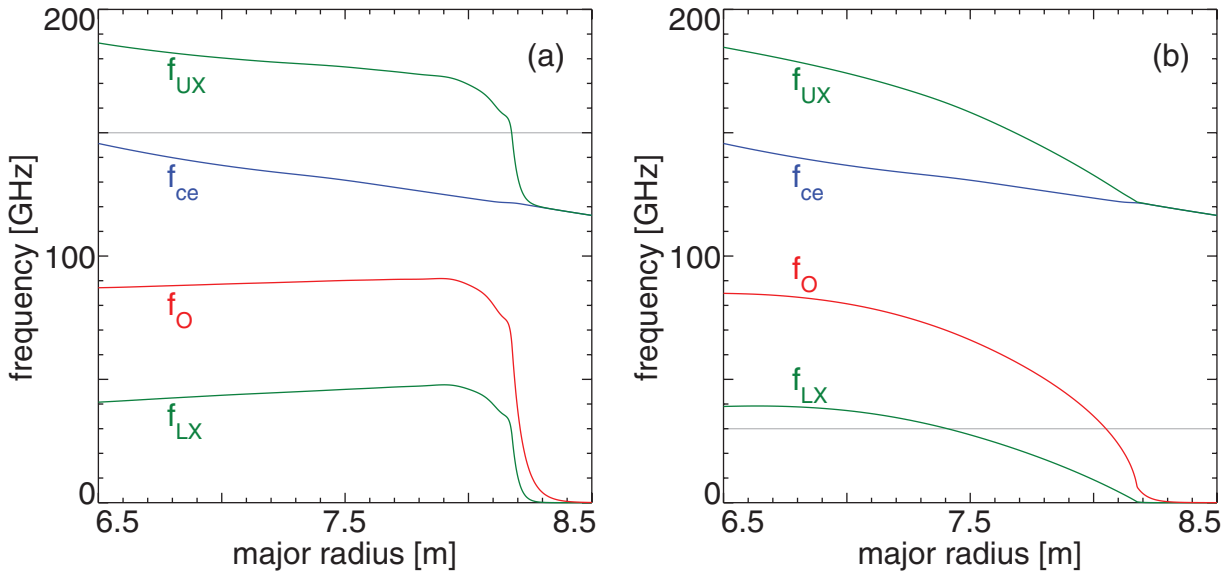

Figure 2. The lower X-mode (f_{LX}), O-mode (f_O), and upper X-mode (f_{UX}) cut-off layers and the electron cyclotron (f_{ce}) resonance as function of major radius used in this paper for (*a*) the 30 GHz O-mode and (*b*) the 150 GHz X-mode simulations.

toroidal directions. Therefore, only a code that solves for the 3D problem can give meaningful results for antenna–plasma coupling simulations.

For the antenna–plasma coupling studies presented in this paper, a new 3D hybrid reflectometer simulation code [7] was used; an outline of the 3D code is given in section 3. The new 3D code is based on a similar approach used in the FWR2D reflectometer code [6].

The antenna–plasma coupling is studied for two microwave frequencies, 30 and 150 GHz, using the equilibrium profiles as discussed in section 2. The results of this study (section 4) show that (i) a vertical array of antennas is needed to cover the vertical variation of the plasma mid-plane relative to the vessel mid-plane, and (ii) only a mono-static antenna system is viable for the ITER LFSR. Most reflectometers that are operational in current fusion research machines use a bi-static antenna set-up with the reflection layer located in the far field. The main advantage of a bi-static system is that only the reflected signal from the plasma is transported to the receiver while the spurious reflections that are often generated in the

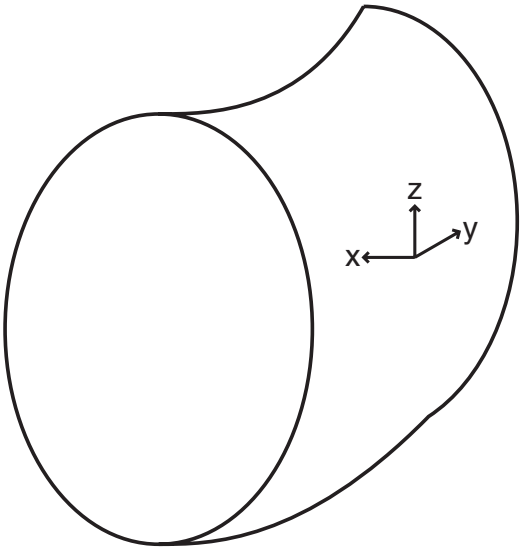

Figure 3. The Cartesian coordinate used in the full-wave 3D code.

transmission lines are absent. A bi-static approach is not feasible in the ITER LFSR due to space restrictions in the ITER port plug and due to the high antenna gain for the higher range of microwave frequencies used.

The degrading effect of density fluctuations in the antenna–plasma coupling is studied in section 5, where it is shown that those fluctuations reduce the reflected power, occasionally leading to the loss of the reflected signal. Such a signal loss can easily be accounted for in the profile measurements because of the high sweep rate—designed to be selectable between 4 and 24 μs per sweep—used for the profile measurements.

In section 6 it is concluded that, based on the 3D reflectometer simulations presented in this paper and after some minor changes to the proposed design of the ITER LFSR, the antenna–plasma coupling of the ITER LFSR is sufficient to meet its specifications.

2. ITER parameters

The primary goal of the LFSR is to provide edge electron density profiles ($r/a > 0.85$) with a spatial resolution 0f 0.5 cm. A number a fast frequency-swept profiles (sweep time: 4–24 μs) will be measured and averaged to a single equilibrium density profile every 10 ms. Density transients such as edge localized modes (ELMs) and L–H transitions should be resolved on a 0.1 ms time scale, which can be obtained by using a shorter time averaging window than for normal profile measurements.

For the antenna–plasma coupling studies presented in this paper a 15 MA ELMy H-mode scenario was used for the X-mode calculations; its shape is shown in figure 1(*a*), together with a vertical antenna arrangement that was considered during the design process.

The frequency profiles for the various cut-offs and resonances for this plasma scenario are shown in figure 2(*a*). Most of the X-mode antenna–plasma coupling simulations in this paper were done at 150 GHz, which is at the high-frequency side of the reflectometer range (30–165 GHz). In this scenario, 150 GHz reflects 3 cm inside the plasma near the top of the density pedestal, as is indicated in figure 2(*a*). At the low end of the reflectometer frequency range 30 GHz was used, with an O-mode polarization and a parabolic density profile, to represent an L-mode plasma. The characteristic reflection layers in this case are shown in figure 2(*b*), where it can be seen that the 30 GHz reflection layer is located 15 cm inside the plasma.

The choice to focus on these two frequencies was motivated by the fact that at 30 GHz the antenna gain is low and the footprint of the reflected signal is extended at the first wall. The footprint decreases with increasing frequency, and at 150 GHz the antenna gain has become very high—resulting in a highly localized reflected footprint, as will be shown in section 4.

3. The 3D reflectometer code

The calculation of the antenna–plasma coupling is a true 3D problem in tokamaks because of the poloidal and toroidal plasma curvature, sheared magnetic field structure, and the radial density and temperature profiles. Therefore, a 3D version of the well established 2D hybrid simulation code, FWR2D, was developed. Analogously to the 2D code, the 3D code also divides the region in which the waves propagate into three sub-regions: (i) a vacuum region, (ii) a paraxial region, and (iii) a full-wave region. This hybrid approach was taken for computational efficiency. In large tokamaks, and especially in ITER, a full-wave simulation from the antenna to the reflection layer and back is computationally too challenging because of the size of the computational domain (of the order of 0.25 m^3) compared to the microwave wavelengths (0.2–1.0 cm), resulting in a typical grid of of 10^7 points.

In the code a transmission antenna is located at a plane outside the plasma—the antenna plane—where the antenna radiation pattern is specified. The waves are propagated from the antenna plane in the vacuum region, located between the antenna plane and the plasma edge, using the Fresnell–Huygens equation. In the region between the plasma edge and a surface close to the reflection layer, called the paraxial region, a paraxial technique [8] is used to propagate the waves to the region where the full wave solution calculated. The effects of the equilibrium plasma and the density fluctuations are taken into account in the paraxial and full-wave regions on the wave propagation. At the boundary between the paraxial and the full wave region, the incoming paraxial solution is used to construct the source for the full wave solution.

In the full-wave region the following wave equation:

$$\frac{\partial^2 \mathbf{E}}{\partial t^2} = c^2 \boldsymbol{\nabla} \times (\boldsymbol{\nabla} \times \mathbf{E}) + \omega^2 \boldsymbol{\chi} \cdot \mathbf{E} + \mathbf{S}(y,z)\delta(x - x_s)\mathrm{e}^{-\mathrm{i}\omega t} \tag{1}$$

for the wave-electric field, $\mathbf{E}$, is solved, with c the speed of light, ω the reflectometer frequency, $\boldsymbol{\chi}$ the electric susceptibility tensor, and $\mathbf{S}(y,z)$ the 2D electric field source at the paraxial full-wave boundary located at x_s. The equation is solved in a Cartesian coordinate system with x aligned in the major radius direction, y in the toroidal direction, and z in the

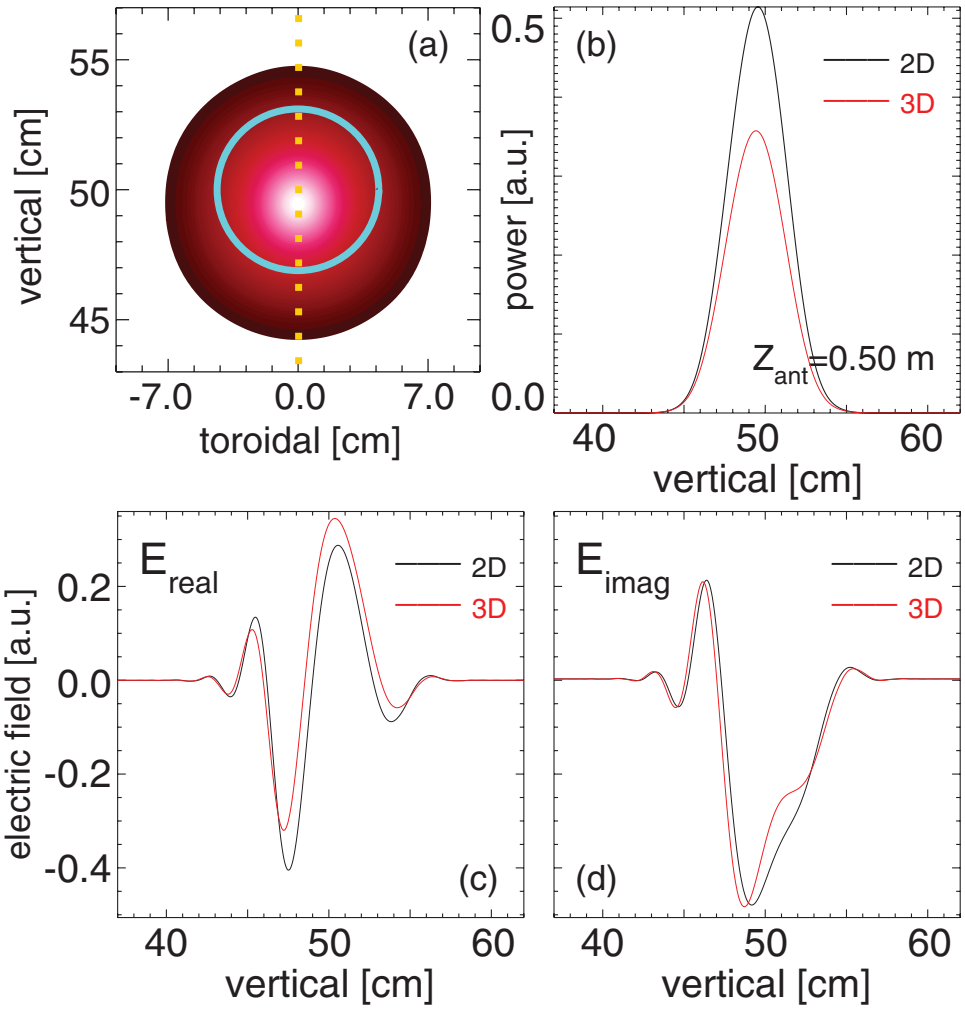

Figure 4. (*a*) Reflected power distribution at the antenna plane for a 150 GHz beam launched from a circular antenna (blue circle) located 2 cm below the plasma mid-plane. (central white: 0 dB, black at the edge: −30 dB). (*b*) Comparison between the reflected power distribution as calculated from the 2D code (black) and 3D code (red) along the symmetry plane indicated with the yellow dots in (*a*). Real (*c*) and imaginary (*d*) electric field comparison for the 2D and 3D results at the symmetry plane.

vertical direction, as shown in figure 3. The electric susceptibility tensor is given in Stix coordinates [9] by:

$$\chi = \begin{pmatrix} \frac{-\omega_p^2}{\omega^2-\Omega_e^2} & -i\frac{\Omega_e}{\omega}\frac{\omega_p^2}{\omega^2-\Omega_e^2} & 0 \\ i\frac{\Omega_e}{\omega}\frac{\omega_p^2}{\omega^2-\Omega_e^2} & \frac{-\omega_p^2}{\omega^2-\Omega_e^2} & 0 \\ 0 & 0 & \frac{\omega_p^2}{\omega^2} \end{pmatrix} \quad (2)$$

with ω_p the plasma frequency and Ω_e the electron cyclotron frequency. Relativistic expressions as discussed in [10–12] are included in the calculation of χ.

In the full-wave region the electric field from the source is propagated to the reflection layer and back beyond the paraxial full-wave boundary. When the full wave solution has reached steady state in the full-wave region, the outgoing full wave is then used as the source for the returning wave through the paraxial and vacuum regions back to the antenna plane and stored for post-processing.

Waves can be launched both in O-mode and in X-mode polarization and propagated to the full wave region. Although coupling between the two polarizations can occur in the full-wave region, a single polarization is extracted at the full-wave paraxial boundary and propagated back to the antenna plane.

A comparison between the well established 2D code and the new 3D codes reveals that the 3D code reproduces the 2D results well, as can be seen in figures 4 and 5 where the reflection of the 2D code is compared with the 3D results. The standard equilibrium as discussed before was used without the poloidal field, so as to keep the fieldline pitch the same in the 2D and 3D simulations. As shown in figure 4(*a*), the transmitting antenna, indicated by the blue circle, is located two centimeters below the plasma mid-plane (the 3D reflected power is shown in red). The vertical power distribution (figure 4(*b*)) and (complex) electric field (figures 4(*c*) and (*d*)) are compared for the 2D calculation and the 3D calculation along the toroidal symmetry line (yellow dots in figure 4(*a*)). The power distribution peaks at the same vertical location for both calculations, although the 3D power is lower than 2D power—which can be explained by the fact that the 3D power is spread in both the toroidal and vertical directions while in the 2D calculation the power is only distributed in the

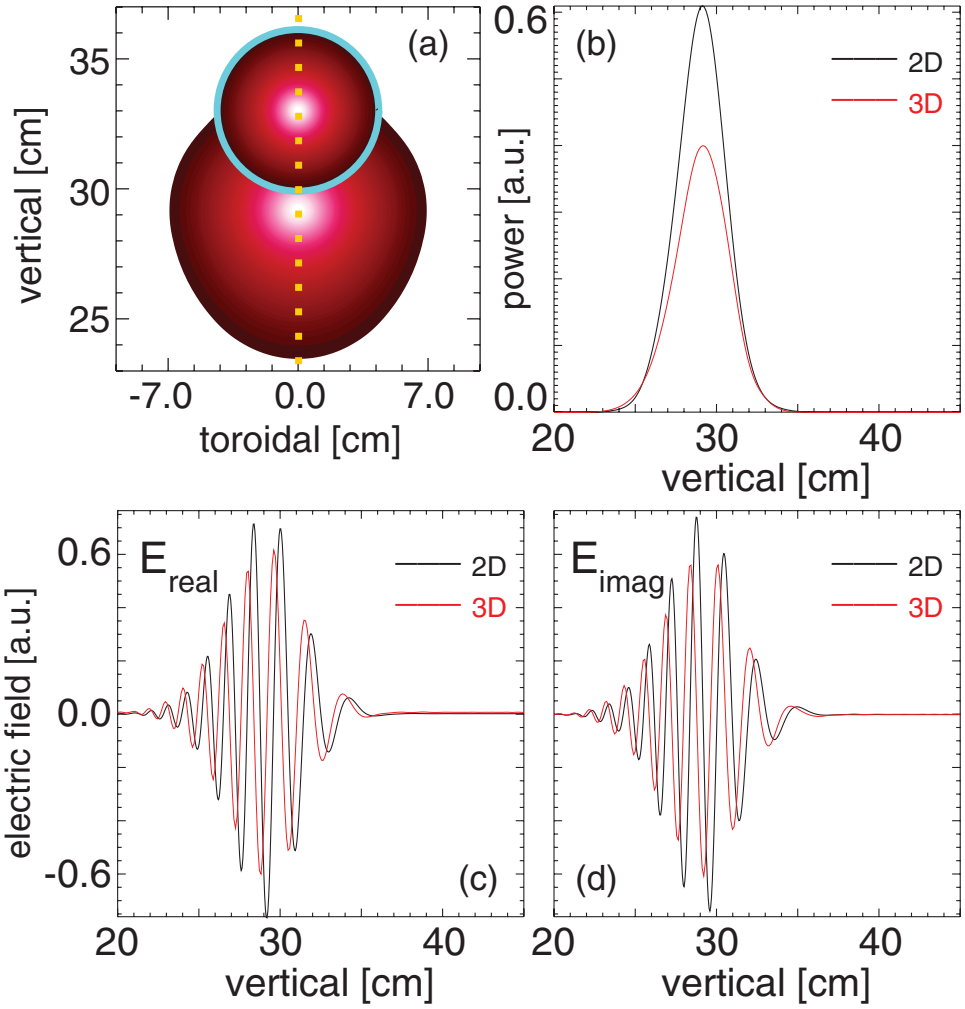

Figure 5. (*a*) Reflected power distribution at the antenna plane for a 150 GHz beam launched from a circular antenna (blue circle) located 19 cm below the plasma mid-plane (central white: 0 dB, black at the edge: −30 dB). The power distribution of the emitted waves is indicated in the antenna aperture. (*b*) Comparison between the reflected power distribution as calculated from the 2D code (black) and 3D code (red) along the symmetry plane indicated with the yellow dots in (*a*). Real (*c*) and imaginary (*d*) electric field comparison for the 2D and 3D results at the symmetry plane.

vertical direction. The electric field distributions agree very well between the 2D and 3D calculations (figures 4(*c*) and (*d*)). They vary slowly with the vertical height, as is expected from a reflection coming from a highly collimated beam that is almost perpendicular to the reflection layer.

A similar result is obtained when the antenna is displaced down by 17 cm, as can be seen in figure 5. In this case the beam is reflected downward (figure 5(*a*)) and the peak of the reflected power has moved from the antenna center at 33 cm–29 cm in both the 2D and 3D calculations (figure 5(*b*)). This shift is caused by the plasma curvature, and results in a strongly varying electric field for both the 2D and 3D calculations as can be seen in figures 5(*c*) and (*d*).

Field-line tracing has shown that a Gaussian beam pattern is returned as a tilted ellipse with the tilt of the ellipse set by the field-line pitch at the reflection layer [13]. When a finite poloidal magnetic field component is included in our 3D calculations we also find that a launched Gaussian beam pattern is returned as a tilted ellipse, as is shown in figure 6 for a 30 GHz O-mode polarized beam. This tilt agrees well with ray-tracing calculations that were performed with the GENRAY code [14, 15] as can be seen as yellow diamonds in figure 6. The ellipse is caused by the anisotropy between the X- and O-mode polarized refraction indices. For O-mode polarization the long axis of the ellipse is perpendicular to the field lines at the reflection layer, while for X-mode polarization the long axis of the ellipse is parallel to the field lines at the reflection layer, albeit much less pronounced than it is for O-mode polarization.

4. Antenna–plasma coupling

As mentioned earlier, the reflectometer antennas cannot be placed far enough from the plasma edge, so that the plasma is in the far field of the antennas—starting between 0.8 and 4.0 m, depending on the frequency. In the current design, the distance between the antennas and the nominal last closed flux surfaces is 25 cm. The reflectometer antennas will consists of a straight piece of circular (6.35 cm in diameter) corrugated wave guide of between 1.3 and 1.9 m depending on

the antenna, connected in the port plug to the transmission line outside via two miter bends. The antenna edges have to be actively cooled to remove the radiation and nuclear heat, and the minimum separation between antenna edges therefore cannot be smaller than 2 cm. Due to these spatial constraints and the high gain of the antennas it is not possible to use a bi-static antenna system for the LFSR system, as is discussed below.

In figures 4(*a*) and 5(*a*) it is shown that the foot-print of the 150 GHz beam reflected at the H-mode plasma edge is only slightly larger than the transmission antenna aperture. For a bi-static configuration at 150 GHz with the transmit and receive antennas 11 cm separated toroidally at the plasma mid-plane, there is no bi-static coupling between the two antennas, as can be seen in table 1, whereas the mono-static coupling in this case is excellent. In order to explore the possibilities for a bi-static system further we have varied the distance between the transmitting and receiving antennas, and the tilt angle of the antennas, as shown in table 1. When the antennas are tilted toward each other, the bi-static coupling improves at the expense of the mono-static coupling but the bi-static coupling stays more than 20 dB below the optimal mono-static coupling.

Because the LFSR is a critical diagnostic for plasma edge density measurements, redundancy should be built into the system in such a way that if one of the antennas fails, the remaining antennas should still give the requested information. In considering a bi-static set-up and the limited port space for mounting antennas, the natural redundancy for a pair of bi-static antennas is the ability to use a single antenna in a mono-static way. Obviously, when a bi-static antenna pair is mounted at 8.48 m this redundancy is lost.

When the antennas are moved back by 30 cm from their nominal position, both bi-static and mono-static coupling can be achieved for the plasma edge (see table 1). Moving the antennas backward decreases the mono-static coupling while increasing the bi-static coupling, while tilting the antennas toward each other increases the bi-static coupling further—albeit at the expense of the mono-static coupling. Moving the antennas closer together and optimizing the antenna tilt improves both the bi-static and mono-static coupling further, although at 7 cm antenna center separation the antennas are already too close to satisfy the cooling geometry constraint.

From the above considerations it is concluded that a bi-static system for the high frequencies of the LFSR is not possible for the following reasons: (i) the bi-static coupling is much lower compared to mono-static coupling; (ii) the redundancy in the antenna system is lost for a bi-static system; and (iii) due to space limitations in the port plug, it is not possible to recess the antennas sufficiently to construct a viable bi-static LFSR system.

At the low-frequency range of the LFSR, coupling between separate transmit and receive antennas is possible as is shown in figure 7. The mono-static coupling for reflections from the equilibrium profiles without fluctuations in this case is −12.3 dB, while the bi-static coupling between the five other proposed antennas varies between −21.0 and −40.5 dB as indicated in figure 7. Although a bi-static antenna arrangement is possible for the lower frequencies of the LFSR, the coupling is still weak compared to the mono-static arrangement—and when density fluctuations are taken into account, the bi-static coupling decreases (as will be discussed in section 5).

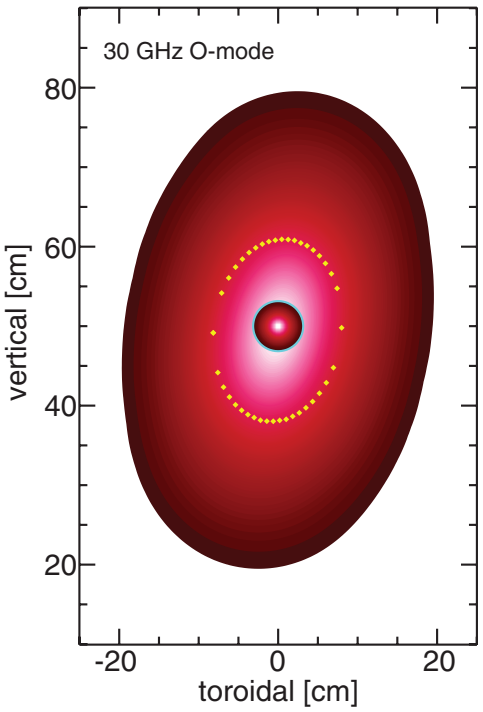

Figure 6. The power distribution at the antenna plane for a 30 GHz beam launched from a circular antenna (blue circle) located 2 cm below the plasma mid-plane showing elliptical deformation and tilt of the reflected signal. The yellow diamonds are obtained from ray-tracing calculations using the GENRAY code.

The plasma mid-plane in ITER is nominally located at 50 cm above the machine mid-plane, but depending on the discharge scenario the plasma mid-plane can vary from about 25–70 cm. The reflectometer system must have the capability to cover this range. In [16] it was argued from 2D reflectometer simulations that a vertical array of antennas is an optimal solution to cover that range. With the 3D code we can now quantify how much the antenna–plasma coupling degrades as a function of the distance between the antenna and the plasma mid-plane, as is shown in figure 8. When the antenna is located at the plasma mid-plane, optimal coupling is obtained for both the low-frequency range (represented by 30 GHz in figure 8) and the high-frequency range (150 GHz) of the LFSR.

The antenna–plasma coupling for low frequencies varies by about 3 dB over the range where the antennas can be mounted because the wave guide that forms the antenna acts as a low-gain antenna at those low frequencies. At high frequencies the wave guide antenna has a much higher gain, and the antenna–plasma coupling is therefore much more strongly peaked around the plasma mid-plane.

When the plasma mid-plane is shifted in ITER from its nominal place, the coupling with the LFSR at the higher frequencies is quickly lost for an antenna fixed at the machine mid-plane, as can be seen in figure 8. A vertical array can overcome this problem, and in the design of the LFSR system studied in this paper two additional antennas—one at 33 cm

Table 1. Bi-static antenna–plasma coupling for the nominal location (8.48 m) and 30 cm further retracted from the plasma for 150 GHz and reflection from the cut-off located at 8.17 m. The two antennas were located at the plasma mid-plane, separated in the toroidal direction (second column), and tilted towards each other with an angle given in the third column. The mono-static coupling is calculated with the same tilt angle as given in column three.

Antenna location (m)	Antenna separation (cm)	Antenna tilt (deg)	Mono-static coupling (dB)	Bi-static coupling (dB)
8.48	11	0.0	−2.7	<−110
8.48	11	±5.0	<−110	−24
8.78	11	0.0	−4.9	−59
8.78	11	±2.0	−26	−22
8.78	9	±1.5	−17	−18
8.78	7	±1.5	−17	−10
8.78	7	±1.0	−10	−14

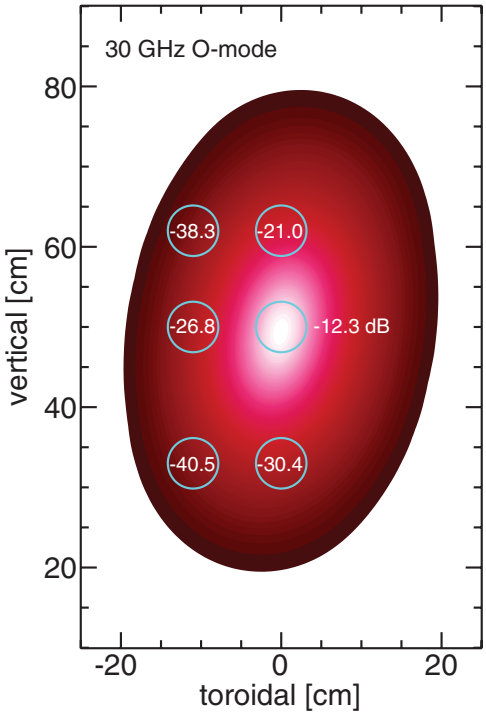

Figure 7. Antenna–plasma coupling for a 30 GHz beam launched at the antenna located toroidally at 0 cm and vertically at 50 cm. The mono-static coupling is −12 dB while the bi-static coupling for the five other antennas varies between −21 and −40 dB.

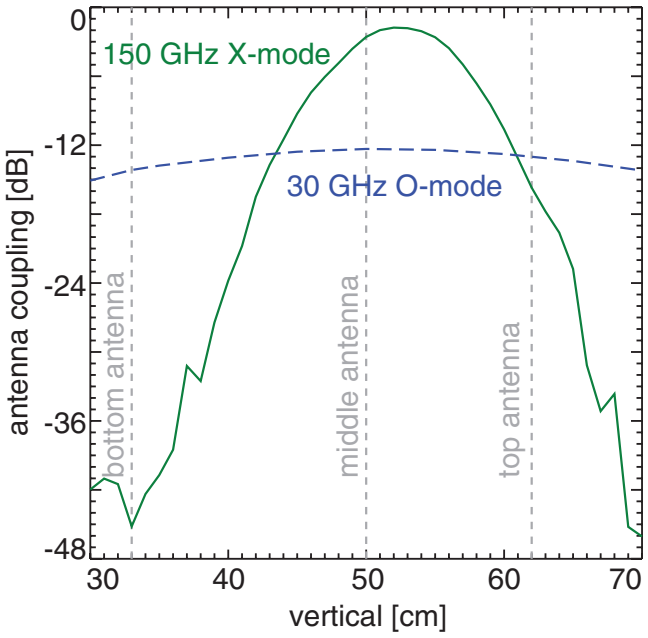

Figure 8. Mono-static antenna–plasma coupling for 30 GHz O-mode (dashed) and 150 GHz X-mode (solid) as function of vertical antenna location for a plasma with its mid-plane at 53 cm.

and the other at 62 cm—were envisioned. In our simulations we have found that the gap between the 33 cm and 50 cm antennas is somewhat too big to obtain a good antenna–plasma coupling when the plasma mid-plane is around 42 cm. Based on these simulations the antennas in the final design will be arranged in a four-antenna vertical array with antenna centers at 0.273, 0.383, 0.493, and 0.643 m above the mechanical mid-plane of the ITER vacuum vessel. This arrangement is sufficient to cover the expected plasma mid-plane displacements in ITER.

One of the main objectives for the ITER LFSR is to measure edge density profiles, but when the plasma density is low enough the reflection layers are located further inside the plasma. The antenna–plasma coupling from well inside the plasma was studied by varying the density gradient of a linear density profile from 10^{19} m^{-4} to 10^{21} m^{-4}. At the low end of this density gradient range the reflections come from deep inside the plasma near the core, while at the high density gradients the reflection is localized at the plasma edge, as can be seen in figure 9. The antenna–plasma coupling decreases when the reflection layer moves inward. The power from the X-mode reflection at 150 GHz is somewhat higher than the decrease in power that can be expected from a plane mirror. This can be understood from the fact the X-mode waves are reflected from slightly concave vertical reflection layers. The concave curvature is caused by relativistic effects due to the high electron temperatures as was shown in [16]. In this density scan simulation we have used a parabolic electron temperature that reached 20 keV at the magnetic axis.

The O-mode antenna–plasma coupling decreases faster than the expected decrease from a plane mirror (figure 9), which is due to the convex shape of the O-mode reflection layer. When the density profile is favorable, (i.e. no steep edge gradient and a non-zero density gradient inside the plasma) reflectometer measurements can be made near the core. For

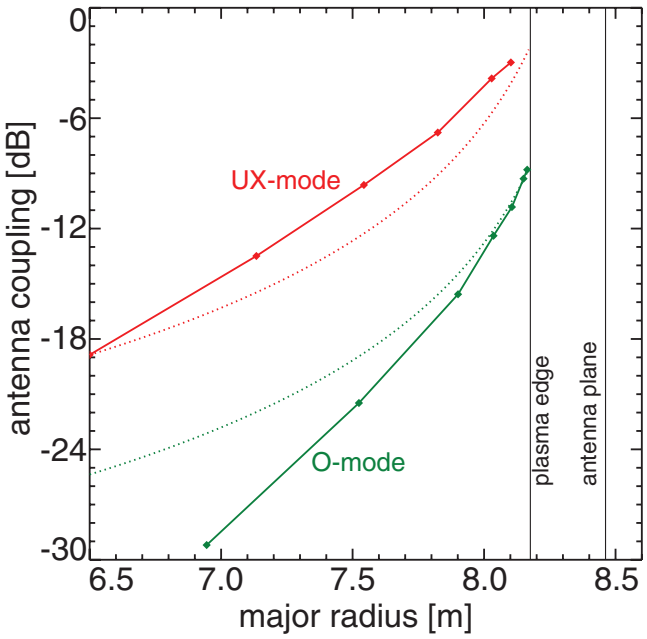

Figure 9. The antenna–plasma coupling decreases when the reflection layer is localized deeper in the plasma: (red) 150 GHz UX-mode (green) 30 GHz O-mode. The dotted curves indicate the expected coupling for propagation in free space and reflection from a plane mirror.

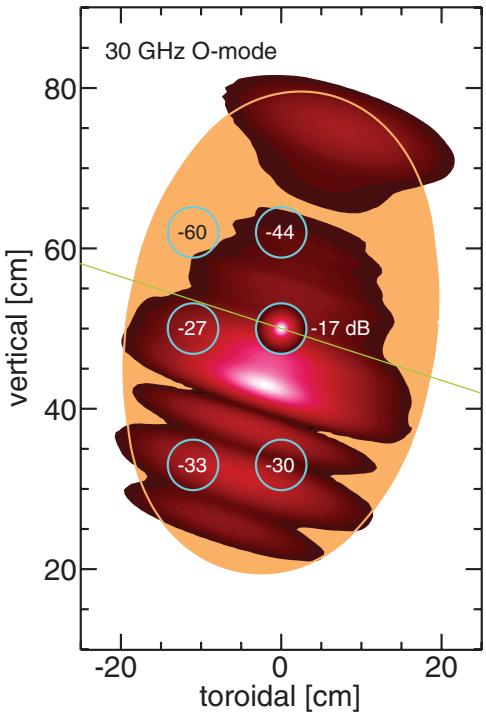

Figure 10. Reflected power foot-print (red) for a 30 GHz O-mode beam when density fluctuations are included ($\Delta k_r = \Delta k_z = 1$ cm^{-1}, $\tilde{n}/n = 5\%$). Microwaves are launched at the antenna located toroidally at 0 cm and vertically at 50 cm. The equilibrium footprint is shown as the orange ellipse, while the antenna coupling is indicated for the same six antennas as shown in figure 7. The green line shows the magnetic field line pitch at the reflection layer.

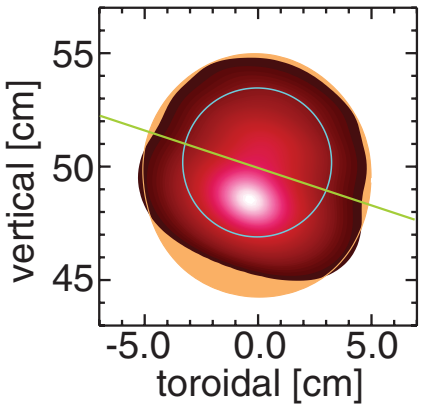

Figure 11. Reflected power footprint (red) for a 150 GHz X-mode beam when density fluctuations are included ($\Delta k_r = \Delta k_z = 1$ cm^{-1}, $\tilde{n}/n = 1\%$). The equilibrium foot-print is shown as the orange ellipse while the green line shows the magnetic field line pitch at the reflection layer.

this purpose the X-mode polarization is better suited than the O-mode polarization because of the focusing effect of the reflection layer.

5. Fluctuation effects on antenna–plasma coupling

So far, only reflections from the equilibrium profiles have been considered—but density fluctuations can modify the reflectometer performance significantly [17, 18]. The 3D reflectometer code has been written in such a way that statistically relevant ensembles of plasma fluctuations can be generated and their effects on the reflected signal studied. In the calculations presented below, a spectrum of Gaussian density fluctuations was included in the 3D reflectometer code. The fluctuation in the radial and vertical direction are centered at wave numbers k_r and k_z with Gaussian widths of Δk_r and Δk_z respectively, while the fluctuations in the toroidal direction are aligned along the field lines with $k_{\|} = 0$ cm^{-1} and $\Delta k_{\|} = 0$ cm^{-1}.

The effect of density fluctuations is well visible on the footprints of the reflected signals for the 30 GHz O-mode (figure 10) and 150 GHz X-mode (figure 11) calculations.

For the O-mode case the effects of a density fluctuation realization from a spectrum with $k_r = k_z = 0$ cm^{-1}, $\Delta k_r = \Delta k_z = 1$ cm^{-1}, and $\tilde{n}/n = 5\%$—a value that is not uncommon in L-mode plasmas—is shown in figure 10, where it can be seen that the power footprint at the antenna plane is completely distorted. The mono-static coupling for the central antenna has decreased, while the bi-static coupling between the central launch antenna and the surrounding antennas is severely degraded compared to the equilibrium profiles without fluctuations (as was shown in figure 7).

Density fluctuations have a smaller effect on the power footprint for the 150 GHz X-mode polarization, as can be seen in figure 11. In this case the density fluctuation, $\tilde{n}/n$, was set at 1%—a value that is not uncommon in H-mode plasmas—while the wave numbers were kept the same as in the O-mode case.

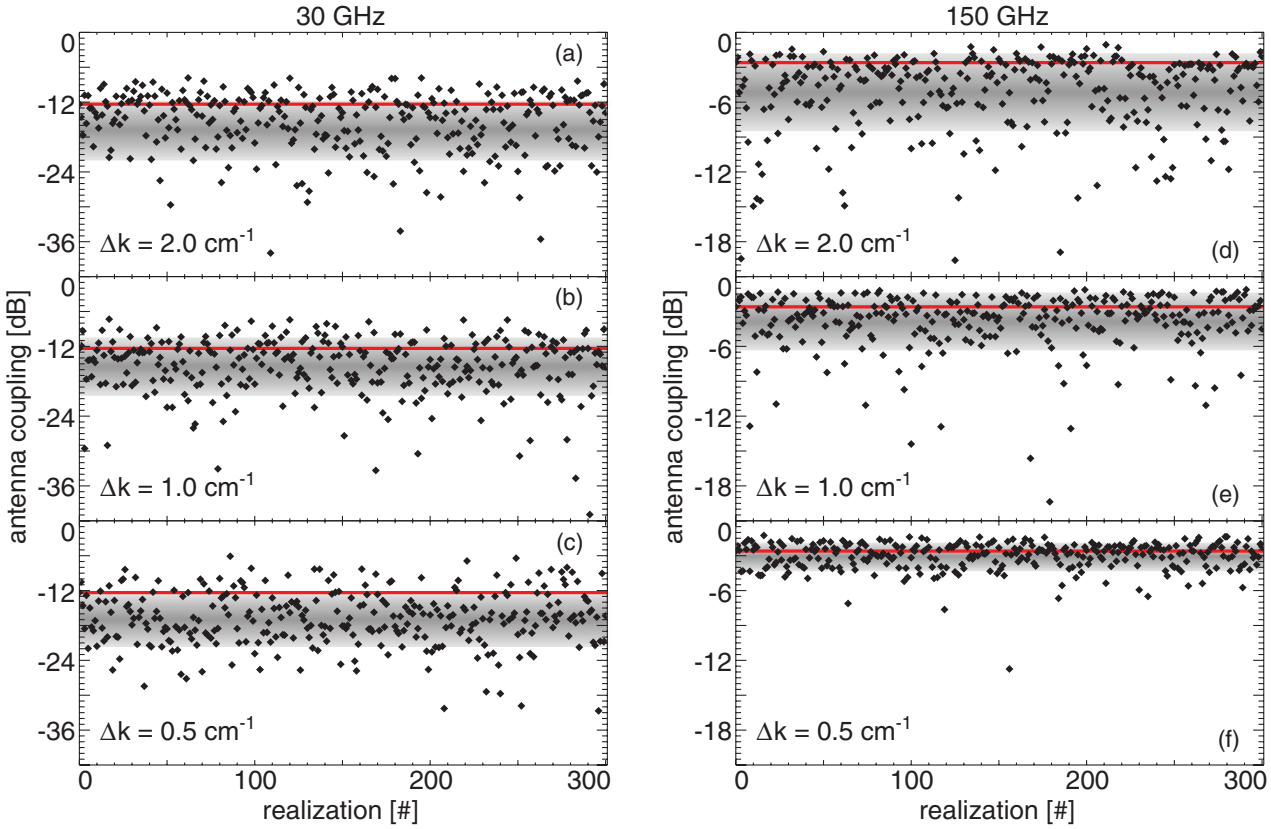

Figure 12. Three hundred realizations for 30 GHz (*a*)–(*c*) and 150 GHz (*d*)–(*f*) with fluctuation wave numbers $\Delta k_r = \Delta k_z = 2.0$, 1.0, and 0.5 cm^{-1}. The density fluctuation level in the 30 GHz O-mode case was set at 5% and at 1% in the 150 GHz X-mode case. The red line is the equilibrium coupling value, while the gray bands indicate the plus and minus one standard deviation around the average fluctuation level. Note the difference in the vertical scale between the 30 GHz and 150 GHz graphs.

Table 2. Mono-static antenna–plasma coupling in the presence of density fluctuations that are isotropic in the radial and vertical direction. A 5% fluctuation level was used for the 30 GHz calculations and a 1% level for the 150 GHz calculations.

Fluctuation wave number (cm^{-1})	Correlation length (cm)	30 GHz Coupling (dB)	150 GHz Coupling (dB)
Equilibrium profiles		−12.35	−2.60
0.5	4.0	-16.84 ± 4.73	-3.03 ± 1.22
1.0	2.0	-15.40 ± 5.02	-3.83 ± 2.48
2.0	1.0	-15.42 ± 5.16	-5.15 ± 3.33

The effects of density fluctuations in the plasma on the antenna–plasma coupling was investigated further by generating 300 independent realizations of the density fluctuations and calculating the coupling for each realization. Fluctuations that were isotropic in the radial and vertical direction were used with three values of Δk: 0.5, 1.0, and 2.0 cm^{-1}. These values correspond to density correlation lengths of four, two, and one centimeter. A density fluctuation level of 5% was used for the 30 GHz O-mode case, while in the 150 GHz X-mode case 1% was used.

The fluctuation level values that are used in the simulations were chosen to represent the high end of density fluctuations that are observed in experiments [19]. A fluctuation parameter scan will not change the conclusions on the antenna–plasma coupling because lower fluctuation levels scatter the microwave power less and the average antenna–plasma coupling will converge to antenna–plasma coupling value that was obtained for the equilibrium plasma profiles.

The results from these calculations (figure 12) show that the fluctuations induce significant variations in the antenna–plasma coupling. Average values and standard deviations for these cases are listed in table 2. In the 30 GHz case the average attenuation due to density fluctuations is 3 dB with a standard deviation of 5 dB for all three values of Δk used. Note that in a number of realizations the coupling becomes very small, which means in practice that the reflected signal at the receiving antenna will be lost in the noise. The antenna–plasma coupling for the 150 GHz case is more sensitive to the fluctuation wave numbers as can be seen in figures 12(*d*)–(*f*). The coupling improves, both in average value and in spread, when the wave numbers decrease (see also table 2).

The different behavior of the antenna–plasma coupling for the 30 GHz and 150 GHz beams can be understood from the large difference in vacuum wavelength, λ_0: 10 mm of 30 GHz and 2 mm for 150 GHz. The width of the last Airy fringe near the turning point, W_{Airy} is given by

$$W_{\mathrm{Airy}} = 0.48 L_n^{1/3} \lambda_0^{2/3} \tag{3}$$

where $L_n = |n/\nabla n|$ is the density scale length at the reflection plane. For the 30 GHz case $W_{\mathrm{Airy}} = 1.2$ cm, which is of the same order of magnitude as the correlation length of

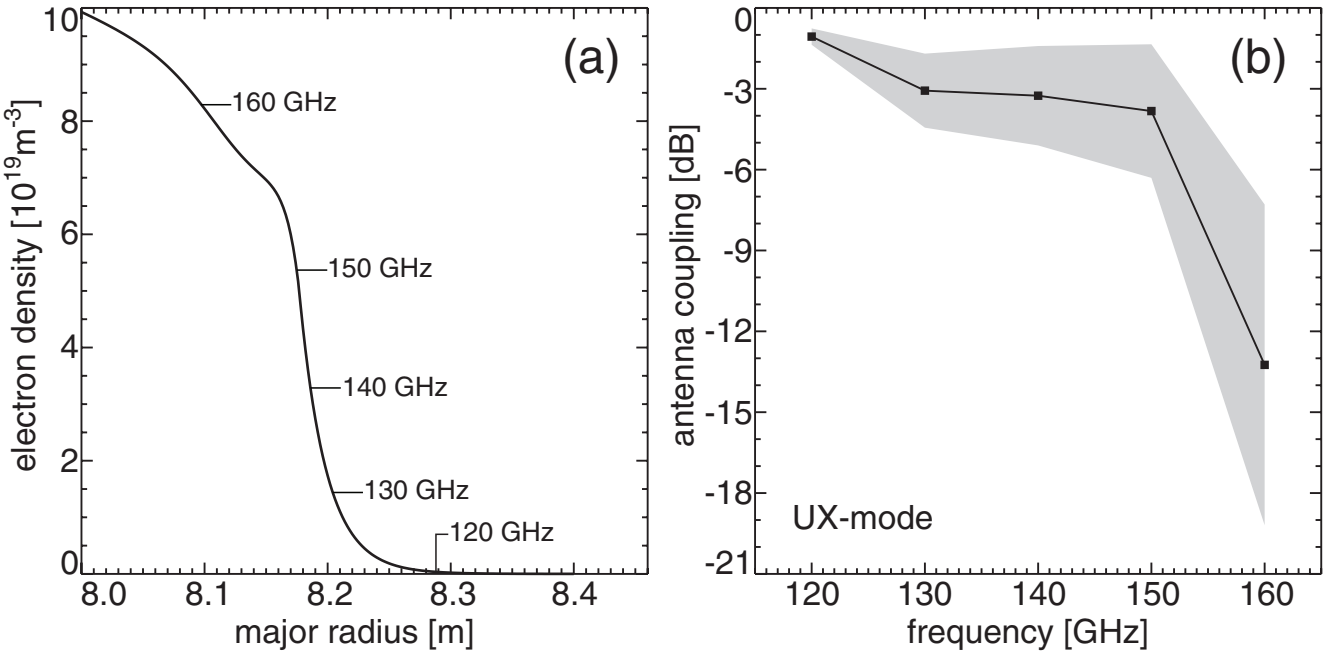

Figure 13. (*a*) H-mode equilibrium density profile with the locations indicated where UX-frequencies reflect that were used to investigate the (*b*) antenna–plasma coupling as function of the reflectometer frequency. The gray band in (*b*) represents the one-sigma variation around the average antenna coupling (solid line). Fluctuation parameters: $\tilde{n}/n = 1\%$ and $\Delta k = 1.0\ \mathrm{cm}^{-1}$.

the density fluctuations, and the reflected signal is therefore strongly affected by the fluctuations, as was shown for the 30 GHz fluctuation footprint in figure 10. For the three different wave numbers studied, the coupling degrades by more than 3 dB compared to the coupling from the equilibrium profile and the standard deviation becomes about 5 dB as is shown in table 2.

The last Airy fringe width in the 150 GHz case is 0.25 cm, which is much smaller than the density correlation lengths used, and the density fluctuations therefore do not affect the coupling as much as in the 30 GHz case, which is also reflected in the 150 GHz footprint shown in figure 11. The plasma–antenna coupling, however, degrades when Δk increases in the 150 GHz simulations as can be seen in figures 12(*d*)–(*f*) and table 2.

Fluctuations affect the reflected power during the fast-frequency sweeps that will be used for profile measurements. The influence of density fluctuations was calculated at several upper X-mode frequencies that cover the plasma edge as is shown in figure 13(*a*). In these calculations an ensemble of 300 realizations was used with $\tilde{n}/n = 1\%$ and $\Delta k = 1.0\ \mathrm{cm}^{-1}$. It can be seen in figure 13(*b*) that the antenna–plasma coupling in the scrape-off layer (120 GHz) and the steep density gradient region is excellent, but that it starts to degrade somewhat beyond the top of the pedestal. The system can cope with such a degradation because for each equilibrium profile which is required every 10 ms, multiple sweeps are averaged after removing unreliable data. We therefore conclude that despite the presence of density fluctuations, the antenna–plasma is sufficient to obtain reliable edge density profiles.

6. Discussion and conclusion

The antenna–plasma coupling has been studied for the ITER low-field side reflectometer with a new 3D hybrid reflectometer code. Before studying the coupling in detail, a benchmark for the results from the 3D code was set using the well established 2D results and ray-tracing calculations. The 3D code was able to reproduce those results correctly, thereby giving confidence in the simulations that were performed for the ITER LFSR.

The antenna–plasma coupling calculations that were done with the equilibrium fields indicate that a bi-static static antenna set-up, which is commonly used in current machines, is not viable for the ITER LFSR because the antenna gain varies strongly over the 30–165 GHz frequency range over which the system should be able to work. At low frequencies, where the antenna gain is low, the footprint of the reflected signal on the wall is large enough to construct a bi-static system, but in the high-frequency range the footprint is too small to couple two adjacent antennas sufficiently strongly to get meaningful signals. Tilting the antennas toward each other improves the coupling but is insufficient for the construction of a reliable bi-static system. Moreover, by tilting the antennas, the possibility of using the antennas in a mono-static configuration

as a fail-safe back-up is lost due to the high gain and antenna tilt. Cooling considerations restrict the minimum distance between antenna pairs to 2 cm, which restricts the design for a bi-static configuration further. Based on the antenna–plasma coupling simulations it was concluded that only a mono-static configuration is viable for the ITER LFSR.

The plasma mid-plane in ITER is allowed to move over about half a meter, while the reflectometer should be able to deliver meaningful measurements over this range. The 3D reflectometer code was used to study the effects of the antenna–plasma coupling over the given plasma mid-plane range. It was found that the vertical separation between two antennas in a three-antenna array is too large to give sufficient coupling when the plasma mid-plane is half-way between the two antennas. In a successive design iteration, a four-antenna vertical array was used to cover that blind spot.

Plasma density fluctuations have in general a detrimental effect on the antenna–plasma coupling, because they scatter power away from the receiving antenna. The 3D reflectometer code was also used to quantify the effects of density fluctuations on the coupling. It was found that the effects of density fluctuations at low frequencies is more harmful than at high frequencies because of the difference in wavelength of the probing waves. The degradation of the antenna–plasma coupling will be included in the power loss calculations for the LFSR.

Based on the 3D reflectometer simulations presented in this paper, the antenna–plasma coupling of the ITER LFSR is strong enough to obtain data that can meet the design specifications. The ultimate success of the system, however, depends also on the engineering of the microwave sources and the transmission lines, which is beyond the scope of this paper [20].

Acknowledgments

This work has been conducted under DOE Contract No. DE-AC02-09CH11466.

References

[1] Vayakis G. *et al* 2006 *Nucl. Fusion* **46** S836
[2] Nazikian R., Kramer G.J. and Valeo E.J. 2001 *Phys. Plasmas* **5** 1840
[3] Kim K.W., Doyle E.J., Peebles W.A., Ejiri A., Luhmann N.C. Jr and Rettig C.L. 1995 *Rev. Sci. Instrum.* **66** 1229
[4] Kramer G.J., Nazikian R. and Valeo E.J. 2003 *Rev. Sci. Instrum.* **74** 1421
[5] Nazikian R. *et al* 2005 *Phys. Rev. Lett.* **94** 135002
[6] Valeo E.J., Kramer G.J. and Nazikian R. 2002 *Plasma Phys. Control. Fusion* **44** L1
[7] Valeo E.J., Kramer G.J. and Nazikian R. 2009 3D full-wave simulations of reflectometry *AIP Conf. Proc.* vol 1187, ed V Bobkov and J-M Noterdaeme (New York: American Institute of Physics) pp 649–52
[8] Smirnov A.I. and Petrov E.Yu. 1999 Electromagnetic wave beams in an inhomogeneous magnetoplasma *26th EPS Conf. on Controlled Fusion, Plasma Physics (Maastricht, 14–18 June 1999)* vol 23J pp 1797–800 (http://epsppd.epfl.ch/Maas/web/sessions.htm#p4113)
[9] Stix T.H. 1992 *Waves in plasmas* (New York: AIP) p 7
[10] Mazzucato E. 1992 *Phys. Fluids* B **4** 3460
[11] Bindslev H. 1992 *Plasma Phys. Control. Fusion* **34** 1601
[12] Bindslev H. 1993 *Plasma Phys. Control. Fusion* **35** 1093
[13] Gourdain P.-A. and Peebles W.A. 2008 *Plasma Phys. Control. Fusion* **50** 025004
[14] Smirnov A.P. and Harvey R.W. 1995 *Bull. Am. Phys. Soc.* **40** 1837
[15] Bertelli N. *et al* 2012 *Phys. Plasmas* **19** 082510
[16] Kramer G.J., Nazikian R., Valeo E.J., Budny R.V., Kessel C. and Johnson D. 2006 *Nucl. Fusion* **46** S846
[17] Sips A.C.C. and Kramer G.J. 1992 *Plasma Phys. Control. Fusion* **35** 743
[18] Gusakov E.Z. and Popov A.Yu. 2002 *Plasma Phys. Control. Fusion* **44** 2327
[19] Fonck R.J., Cosby G., Durst R.D., Paul S.F., Bretz N., Scott S., Synakowski E. and Taylor G. 1993 *Phys. Rev. Lett.* **70** 3736
[20] Muscatello C 2018 Development of a 30–165 GHz density profile reflectometer and performance evaluation for ITER *Rev. Sci. Instrum.* in preparation